ACS NANO

www.acsnano.org

ARTICLE

Hyperspectral Detection of the Fluorescence Shift between Chirality-Sorted Empty and Water-Filled Single-Wall Carbon Nanotube Enantiomers

Maksiem Erkens, Wim Wenseleers,* Miguel Ángel López Carrillo, Bea Botka, Zohreh Zahiri, Juan G. Duque, and Sofie Cambré*

Cite This: *ACS Nano* 2024, 18, 14532−14545

Read Online

ACCESS | Metrics & More | Article Recommendations | Supporting Information

ABSTRACT: Single-wall carbon nanotubes (SWCNTs) have extraordinary electronic and optical properties that depend strongly on their exact chiral structure and their interaction with their inner and outer environment. The fluorescence (PL) of semiconducting SWCNTs, for instance, will shift depending on the molecules with which the SWCNT's hollow core is filled. These interaction-induced shifts are challenging to resolve on the ensemble level in samples containing a mixture of different filling contents due to the relatively large inhomogeneous line width of the ensemble SWCNT PL compared to the size of these shifts. To circumvent this inhomogeneous broadening, single-tube spectroscopy and hyperspectral imaging are often applied, which until now required time-consuming statistical studies. Here, we present hyperspectral PL microscopy combined with automated SWCNT segmenting based on either principal component analysis or a convolutional neural network, capable of both spatially and spectrally resolving the PL along the length of many individual SWCNTs at the same time and automatically fitting peak positions and line widths of individual SWCNTs. The methodology is demonstrated by accurately determining the emission shifts and line widths of thousands of left- and right-handed empty and water-filled SWCNTs coated with a chiral surfactant, resulting in four statistical distributions which cannot be resolved in ensemble spectroscopy of unsorted samples. The results demonstrate a robust method to quickly probe ensemble properties with single-enantiomer spectral resolution. Moreover, it promises to be an absolute quantitative method to characterize the relative abundances of SWCNTs with different handedness or filling content in macroscopic samples, simply by counting individual species.

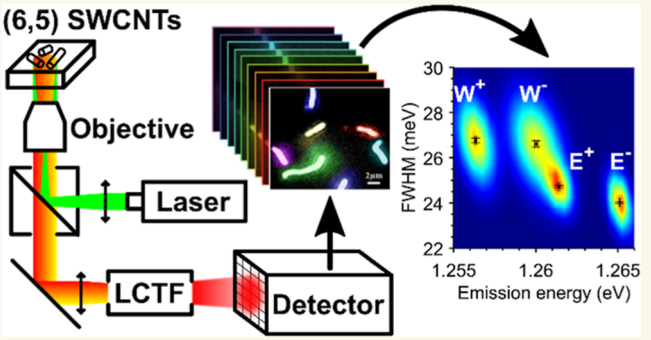

KEYWORDS: *hyperspectral microscopy, single-wall carbon nanotubes, aqueous two-phase separation, density gradient ultracentrifugation, fluorescence, enantiomer*

INTRODUCTION

A detailed understanding of the strongly chirality-dependent electronic, optical, and vibrational properties of single-wall carbon nanotubes (SWCNTs) is key for unlocking their true potential.[1] One of the great assets in advancing the understanding of these properties has been the range of optical spectroscopic techniques[1] that is particularly powerful for their characterization, such as absorption spectroscopy, photoluminescence-excitation (PLE) spectroscopy, and (wavelength-dependent) resonant Raman spectroscopy (RRS).[1] In case well-individualized SWCNT samples are studied with consequently reduced SWCNT intrinsic spectroscopic line widths, e.g., using surfactant-based SWCNT dispersions,[2,3] these techniques are readily capable of discriminating the different chiralities from each other based on their well-separated, chirality-specific spectroscopic signals, even in mixed-chirality samples.

Received: February 16, 2024
Revised: April 17, 2024
Accepted: May 2, 2024
Published: May 17, 2024

Aside from the chirality-dependent variations, the SWCNT spectroscopic properties are also easily influenced by interactions with the environment, both from the outside (exohedral) and from the inside of the SWCNT (endohedral). Indeed, depending on the exact wrapper molecule used for dispersion,[4−6] the external adsorption of molecules[7] or the filling type of the nanotube's hollow core[8−13] the SWCNT's fluorescence (PL) shifts in emission wavelength, the PL efficiency can be either reduced or enhanced and the line width changes. However, in general, these spectral shifts are quite small (of the order of 5−20 meV as determined for a wide range of fillers[10]) compared to the intrinsic PL line width (of the order of 10−30 meV), making it impossible to resolve them with ensemble PLE spectroscopy in samples with mixed filler content, where all of these multitudinous, interaction-induced PL shifts are probed simultaneously. This inevitably leads to an additional inhomogeneous broadening of the PLE signals, drastically complicating the characterization of these environment-dependent PL variations and even obscuring the observation of the intrinsic emission properties of SWCNTs. Nevertheless, SWCNTs are envisioned as ideal emitters for highly sensitive biomedical and biochemical sensors,[7,14−17] where the sensitivity is based on the detection of emission changes in different environments (e.g., pH, molecular adsorption, etc.). Thus, a method to quantify these shifts in a robust and automated manner with single-tube precision while providing fast and enough statistics is needed.

Only if adequately sorted SWCNT samples are investigated, where the different possible environmental interactions among the nanotubes have been well isolated from each other, or in single-tube spectroscopic measurements, it becomes possible to characterize these spectral shifts among the different species of the same chirality. For instance, although a dispersion of surfactant-wrapped SWCNTs naturally contains a mixture of empty and water-filled SWCNTs,[13] a shift of approximately 10−15 meV between their emission spectra can be observed with PLE spectroscopy when empty and water-filled tubes are separated from each other by density gradient ultracentrifugation (DGU).[10,18] Similarly, only when studying enantiomer-sorted SWCNTs, an even smaller spectral shift in the optical properties between the left- and the right-handed versions of the same chirality, (n,m) versus (m,n), can be detected on the ensemble level.[19−22] This enantiomeric difference in the optical properties, arises from a variation in the exohedral interactions with the surrounding chiral surfactant molecules, which wrap themselves differently around the chiral nanotube, depending on the nanotube's handedness.[19−22] Indeed, when different molecules are used to disperse the SWCNTs, different shifts in the emission wavelength between the two enantiomers can be observed. In case of (6,5) enantiomers wrapped by the chiral surfactant sodium cholate mixed with sodium dodecyl sulfate and sorted using DGU, for instance, this shift is approximately 4 nm,[21] while a shift of approximately 5 nm has been detected for DNA-wrapped SWCNTs, which disappears when the DNA strands are exchanged with a nonchiral surfactant.[19]

Hence, only by strictly limiting the amount of (endohedral and exohedral) environmental interactions present in the sample, it becomes possible to distinguish different types of interaction-induced spectral variations on the ensemble level. This approach, however, requires detailed sorting protocols that are able to physically separate SWCNTs with different environmental interactions from one another, like the difference in buoyant density between empty and water-filled SWCNTs with DGU.[18] This consequently limits the ensemble study on the possible origins of inhomogeneous broadening to those that can be isolated from each other. Furthermore, the accuracy of the obtained spectral shifts is limited by the sorting purity, as these separations are never complete, in particular for small-diameter SWCNTs. For example, there will always be a small residue of empty SWCNTs in the more dense water-filled fraction of DGU sorted SWCNTs due to the fact that for small diameters the spatial distribution of both species overlaps because of diffusion.[23] Moreover, in particular, for sensing applications, such required separation steps cannot always be integrated, making a different methodology to assess the environmental changes needed.

In this work, we, therefore, combine hyperspectral imaging with automated SWCNT structure recognition and spectral analysis. In hyperspectral imaging, multiple images are recorded as a function of wavelength in order to acquire a multidimensional image that contains both the spatial and spectral information on the SWCNTs in a multidimensional data cube, the so-called hyperspectral image (HSI).[24−26] Two dimensions of this HSI represent the projected spatial dimensions of the imaged object, providing similar information as optical wide-field fluorescence microscopy. The latter indeed can visualize individual fluorescing SWCNTs by their length and has proven to be an impactful method to probe the polarization dependent excitation of SWCNTs,[27] to perform dynamical studies on the Brownian motion of SWCNTs in a liquid,[28,29] to estimate the exciton dynamics,[30] to reveal filling of SWCNTs along their length,[31] and to detect spatially localized PL quenching sites.[32] In fact, SWCNTs have even been found to be ideal chromophores for super-resolution imaging in biological tissue.[29,33] The other dimensions of the HSI contain the spectral information on the individual SWCNTs, thereby combining spatial and spectral information in one image. Previous single-tube spectroscopy experiments, measuring one tube after another, revealed the SWCNT interactions with their exohedral and endohedral environment even along the length of an individual nanotube.[8,14,32] In contrast with these previous works, however, statistical information can be directly extracted from the HSI, as many individual SWCNTs can be imaged simultaneously, thereby reducing the collection times significantly. Such a hyperspectral microscopy approach has, for instance, already successfully led to the detection of localized defect-emission sites along the nanotube's length and the brightening of local dark sites upon application of a strong magnetic field[34] as well as revealed the spatial distributions of different SWCNT chiralities in living cells,[35] or was used to determine the molecular sieving capability of SWCNT pores.[31] While hyperspectral imaging itself is nowadays commonly used for investigating the interactions of SWCNTs with their environment, statistical studies are, however, typically limited to only a few tens of individual SWCNTs from an entire macroscopic sample. Here, we show that, by combining the HSIs with automated nanotube image recognition, followed by detailed fitting of the PL spectra, this methodology becomes competing in terms of speed with ensemble PLE, providing information on thousands of SWCNTs on a single day, while still having the required single-tube resolution needed to study the environment-induced spectral shifts in the PL. We demonstrate this by using this methodology in combination with aqueous two phase extracted-(ATPE)[36−39] and DGU-sorted[18,40] SWCNT

https://doi.org/10.1021/acsnano.4c02226
ACS Nano 2024, 18, 14532−14545

samples, that serve as ideal reference samples to accurately define the different statistical distributions of empty and water-filled SWCNTs. Moreover, by using a chiral surfactant to coat the SWCNTs, we can even resolve a bimodal splitting of the statistical distribution of both empty and water-filled SWCNTs, identified as the left- and right-handed SWCNTs that each interact differently with the chiral surfactant. Most importantly, note that all chiroptical spectroscopic methods to date cannot provide an absolute quantification of the enantiomeric purity due to the lack of 100% pure samples needed for calibration.[41] In contrast, the present results show promise for an absolute quantification method of the abundance of different enantiomers and their filling state, simply by counting individual species.

RESULTS AND DISCUSSION

Hyperspectral Microscopy Setup. The hyperspectral microscopy setup presented here makes use of an inverted epifluorescence microscope,[42] equipped with a 60-times magnifying oil-immersion objective with numerical aperture 1.4, to image the PL of individual SWCNTs. The SWCNT PL is generated by excitation with a continuous-wave laser, having a fixed wavelength of 568 nm that is chosen specifically to optimally excite (6,5) SWCNTs via their second order optical transition,[2] in a wide-field configuration[42] so that many (at least 20) SWCNTs can be imaged simultaneously. These imaged SWCNTs are surfactant wrapped with the chiral surfactant sodium deoxycholate (DOC) and purposely immobilized in a thin slab of a transparent tetramethyl orthosilicate (TMOS) gel matrix in order to have their entire length in focus while preserving their optical properties with respect to those of SWCNTs in surfactant dispersions (see Figure S1 in the Supporting Information).[43] These SWCNT microscope samples are mounted on top of an XYZ piezo scanning microscope stage to allow for precise positioning and focusing of the sample. The resulting images of the SWCNT PL are recorded with a liquid-nitrogen cooled two-dimensional Si CCD detector (more details can be found in the Methods Section and Section S1 of the Supporting Information).

The spatial resolution of these images is intrinsically determined by the objective's resolving power, which is diffraction limited to 430 nm at the (6,5) SWCNT emission wavelength of approximately 990 nm (using the above-mentioned objective). However, given the pixel size of the detector of 20 μm, combined with the 60-times magnifying objective, each pixel in the final image has a size of 333 nm. According to Nyquist's sampling theorem, for ideal image resolution, the pixel size should at least be two times smaller than the Rayleigh limit, in order that the diameter of the Airy disk can be sampled by 4 pixels. In our case, the image is thus slightly under-sampled, with the ratio of the Rayleigh limit and the pixel size to be 1.3. Experimentally, we find a typical full-width-at-half-maximum (fwhm) of a cross-section of a SWCNT in our images of 1.87 ± 0.25 pixels, thus corresponding to a typical spatial resolution of 624 ± 80 nm (see Supporting Information, Figure S2). Even though this obviously does not allow to resolve the SWCNT diameter, it is still by far enough to image the nanotube's micrometer-long length.

To enable this microscopy setup to record the images as a function of the SWCNT emission wavelength, needed to construct the desired HSI, a liquid crystal tunable filter (LCTF) is placed in between the microscope's exit port and the detector by duplicating the image plane from the microscope with two identical relay systems (see Supporting Information, Figure S3). The LCTF is positioned close to a duplicated image plane of the microscope so that the light rays from different points in the sample all have the same angle of incidence with respect to the LCTF, resulting in an equal filtering of each point. Note that the filter is mounted close to but not directly in the first duplicated image plane in order not to image imperfections and dust particles on the surfaces of the LCTF, in focus in the final image. The LCTF filter acts as a tunable bandpass filter of which the central transmission wavelength can be continuously varied within the range of 850−1800 nm. The spectral resolution of the hyperspectral microscopy setup is determined by the bandwidth of the LCTF, which steadily increases from approximately 7 to 25 nm with increasing wavelength throughout the entire tunable range (see Figure S4 of the Supporting Information). Around the (6,5) SWCNT PL studied here, the LCTF's bandwidth is only 10 nm while the fwhm of the (6,5) SWCNT PL is approximately 20 nm (see further), hence by far sufficient to spectrally resolve the PL. Indeed, the setup's spectral resolution as well as its good wavelength calibration are demonstrated by measuring the spectrum of an argon calibration lamp with the hyperspectral imaging setup in the same wavelength range as the (6,5) SWCNT PL (see Figure S5, of the Supporting Information).

The LCTF's bandwidth, while providing sufficient resolution to resolve the intrinsic SWCNT emission, additionally allows the strong reduction of excitation powers with respect to other hyperspectral imaging setups that use a narrow-bandwidth volume Bragg grating,[14,17,35] the latter resulting in higher spectral resolutions (image bandwidth ∼3−5 nm; higher than needed for the emission of SWCNTs which intrinsically has larger line widths) at the cost of requiring higher illumination powers for obtaining similar signal-to-noise ratios in the HSIs. Although a direct comparison with the literature data is difficult to make, mainly because of the use of a different excitation wavelength for the excitation (e.g., 725 nm in refs 14, 17, and 35 versus 568 nm in our work), different SWCNT processing conditions (DNA-wrapped versus surfactant-wrapped SWCNTs) and possibly different wide-field illumination spot sizes, the excitation powers used in previous works seem very different from our work (e.g., 1.5 W in ref 17 compared to 30 mW in this work). Note that the 30 mW excitation power at 568 nm used here corresponds to an intensity of approximately 7 W/cm^2, well within the linear excitation regime of individual SWCNTs such that the formation of biexcitons and optically generated trions can be strictly avoided.[44] The LCTF as well as the detector and the piezo scanning stage are all controlled via a graphical user interface written in MATLAB that allows for the automatic acquisition of multiple HSIs at different locations in the microscope samples, significantly increasing the throughput of this hyperspectral imaging setup.

Figure 1 shows an example of such an automatically acquired HSI by means of a representative wavelength slice at 985 nm in panel a and a SWCNT single pixel spectrum (blue) in panel c.

Image Corrections. An as-acquired HSI suffers from possible random spikes due to cosmic rays, background signals (e.g., fluorescence from the microscope slides), as also observed in regular PL spectroscopy, and spatial intensity variations among different pixels (e.g., due to a possibly inhomogeneous illumination), which is also common for

https://doi.org/10.1021/acsnano.4c02226
ACS Nano 2024, 18, 14532−14545

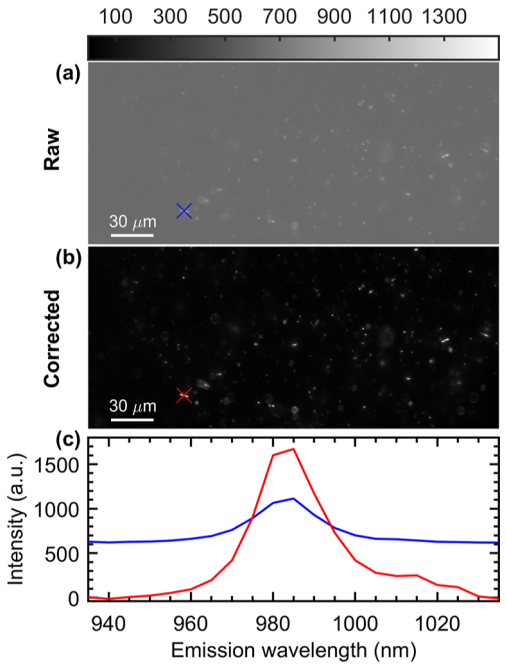

Figure 1. (a) HSI at an emission wavelength of 985 nm before (a) and after (b) applying the image corrections, both presented with the same intensity grayscale. (c) Comparison of a single pixel PL spectrum before (blue) and after (red) the image corrections. The chosen pixel for these spectra is indicated in panels (a,b) by the blue and red cross.

optical microscopy. In order to be able to both spatially and spectrally compare PL intensities in this HSI, it first needs to be corrected for these different types of artifacts and variations prior to the HSI analysis.

First, any possibly present cosmic ray spikes, which are distributed randomly in space and time, are removed by measuring 5 HSIs for each sample position and emission wavelength. As such a temporal multimedian filter can be used on the multiple accumulations acquired for a single emission wavelength. Such a filter sorts the five acquired intensities (of those five HSIs) for each pixel and emission wavelength from low to high and then removes the lowest and highest value after which the average is taken over the remaining 3 intensities. Since these cosmic ray spikes are much more intense than the signals of interest, they are the outliers that are excluded by this algorithm, while also removing the lowest value avoids inducing a bias by the filter. This filter is applied to every image taken, hence also to that of the background and the flatfield.

Next, this filtered HSI, $I(\lambda_{em})$, is corrected for the background, $B(\lambda_{em})$, and the sensitivity of the hyperspectral microscopy setup using the pixel-wise formula

$$I_c(\lambda_{em}) = \frac{I(\lambda_{em}) - B(\lambda_{em})}{F \cdot S(\lambda_{em})} \quad (1)$$

where the setup's sensitivity has been split in a spatially dependent part, F, and a spectrally dependent part, $S(\lambda_{em})$. The background in the HSIs contains contributions from pixel-dependent dark current of the detector but is mostly dictated by the out-of-focus fluorescence of the microscope substrate glass of the sample. As the intensity of this fluorescence not only depends on the imaged wavelength but also on the acquisition parameters (such as integration time, excitation wavelength, alignment, etc.), the hyperspectral background, $B(\lambda_{em})$, is recorded as a HSI analogously to how the SWCNT HSIs are measured, at a position in the sample where no nanotubes are present (see Figure S6, in the Supporting Information for an example).

The spatial sensitivity, also called flatfield F,[45] approximated to be independent of the imaged wavelength, corrects for the nonuniform excitation of the sample. This flatfield is recorded with a thin film of the dye IR-140,[46] which absorbs the excitation laser while fluorescing in the near-infrared range, embedded in a poly(methyl methacrylate) (PMMA) matrix to prevent crystallization of the dye molecules (see Figures S7 and S8 in the Supporting Information). Finally, the spectral sensitivity, $S(\lambda_{em})$, depends mostly on the LCTF transmission at different wavelengths and the sensitivity of the detector and was obtained by measuring a HSI of a calibrated halogen lamp placed out of focus, above the sample's focal plane (see Figure S9 in the Supporting Information). Figure 1b, and the red spectrum in Figure 1c present the corrected HSI at one emission wavelength and a corrected PL spectrum of one pixel, respectively.

Convolutional Neural Network (CNN) for Semantic and Automatic Segmentation. In a typical hyperspectral imaging experiment, about 50 HSIs are collected from random locations in the microscopy samples, with at least 20 SWCNTs per image, easily amounting to information on thousands of SWCNTs acquired in a single day. In the example experiment shown in the next section, for each emission wavelength (from 935 to 1035 nm in 5 nm steps), five accumulations each of 6 s integration time were acquired, resulting in an acquisition time of a full HSI of approximately 11 min. Note that the background and flatfield were recorded once per measurement day. After the automatic image acquisitions and corrections (see above), an automatic statistical analysis of these HSIs is needed. To do so, we implement a procedure that consists of a standardization step to remove any systematic deviations from the spectra,[47,48] a principal component analysis (PCA) step to reduce the dimensionality of the HSI, increasing as such the contrast in the image,[49] such that a segmentation by either a simple Otsu threshold[50] or by a more advanced CNN[51] on this PCA-HSI can help subsequently to identify the pixels belonging to individual SWCNTs.

In the first standardization step, the borders of the image are removed, as these pixels are extremely noisy because of the flatfield correction (i.e., those pixels that are not illuminated and thus divided by 0 in eq 1, see also Figure S8). Subsequently, in every wavelength slice of the HSI, $p(\lambda_{em})$, the median over all the pixels of the image at that wavelength, $m(\lambda_{em})$, is subtracted and afterward divided by the standard deviation of that image, $\sigma(\lambda_{em})$, using the pixel-wise expression

$$p_s(\lambda_{em}) = \frac{p(\lambda_{em}) - m(\lambda_{em})}{\sigma(\lambda_{em})} \quad (2)$$

Since most of the pixels in the HSI are background pixels, they will strongly dictate $m(\lambda_{em})$ and $\sigma(\lambda_{em})$. As such, this standard normal variate normalization[52] reduces the systematic deviations in the spectra either induced by or not well removed by the prior image corrections. This is exemplified in Figure 2 where the pixel spectra of a small part of a HSI (a) before and (b) after standardization are shown, demonstrating that the SWCNT pixels (i.e., those showing an emission intensity) can be more easily recognized after this standardization step.

https://doi.org/10.1021/acsnano.4c02226
ACS Nano 2024, 18, 14532−14545

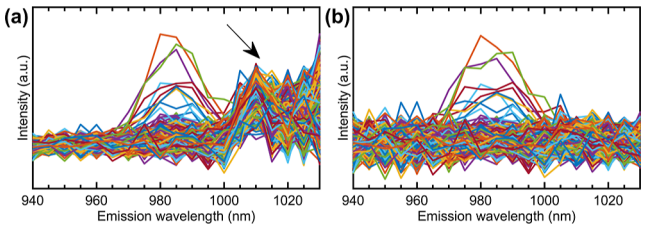

Figure 2. Spectra of all the pixels of a 31 × 31 pixels part of a HSI (a) before and (b) after standardization. Systematic deviations in the spectra, indicated by the arrow, are reduced after standardization. This way, the SWCNT pixels can be more easily recognized.

Subsequently, PCA is applied to these standardized HSIs in order to reduce the dimensionality of these HSIs from 3D to 2D.[49] In short, PCA transforms the wavelength space of the HSI in such a way that the variance in the spatial dimensions of the HSI is maximized. This is beneficial in comparison to simply summing over all the spectral bands of the HSI, as, naturally, the biggest variance in the HSIs arises from the SWCNT pixels, which stand out with respect to the background pixels. Hence, the image of the first principal component (PC1), having the largest variance, will be a linear combination of those wavelength slices in which the SWCNT pixels have a high intensity, making them easier to recognize in the image with respect to the background. Indeed, when comparing the PC1 component with the HSI summed over all wavelengths (Figure 3) a better contrast is obtained in the PC1 image.

However, this PC1 component represents only ∼26% of the total variation, and in fact only holds information on the SWCNTs with the highest intensity. To not exclude weaker emitting SWCNTs from the statistics, PC2 (∼8%) and PC3 (∼5%) are also considered in the subsequent segmentation.

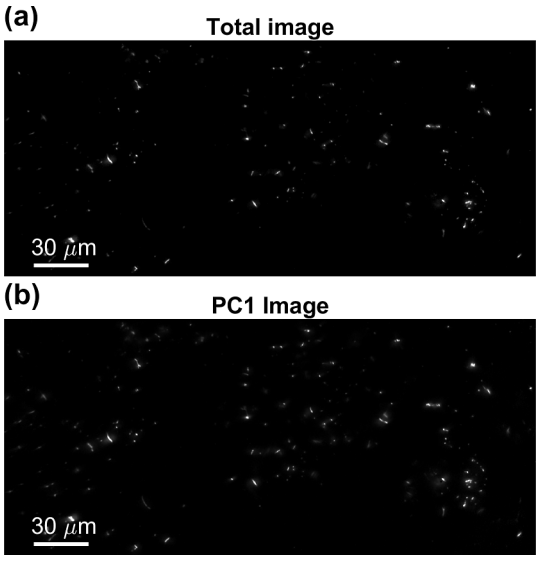

Figure 3. (a) A HSI presented by summing over all the spectral bands. As those wavelength slices without any PL are also included, not all SWCNTs are easily distinguishable from the background. (b) The PC1 image of the same HSI as in panel (a). In both figures, the intensity scale is first normalized and plotted in between [0, 0.4], showing that in the PC1 image, the more weakly emitting SWCNTs have a much better contrast.

These usually have a lower signal-to-noise ratio but allow to segment additional pixels belonging to weakly emitting (sections of) SWCNTs. Combined, PC1, PC2, and PC3 represent, on average, ∼ 39% of the total variation (see Figure S10 in the Supporting Information). Figure S11 in the Supporting Information gives two representative examples of a PC1, PC2, and PC3 image of the same HSI, showing that PC2 and PC3 can hold information on SWCNTs that is not present in the PC1 image. More detailed information on this procedure can be found in Section S3.1 in the Supporting Information.

The PC1, PC2, and PC3 images were then used for further segmentation of the SWCNTs using two different approaches. In a first approach, Otsu's thresholding algorithm is applied individually to each of the three PC images.[50] This method searches for a threshold value that maximizes the intensity variance in the image between the fore- and the background. As the previous PCA already delivered an image in which the variance in between these two image classes is maximized, this approach seemed suitable to segment the PC1, PC2, and PC3 images of the HSIs. While such an Otsu threshold resulted in segmentation of typically about 1000 SWCNTs from a set of 50 HSIs, thus providing nice statistics, it however had drawbacks when using it on images that contain SWCNTs that emit with very different intensities, selecting only the strongest pixel intensities while omitting the less bright pixels from the statistics, such as short SWCNTs, SWCNT segments, and out-of-resonance SWCNT chiralities. Moreover, the Otsu threshold cannot be used to select only those nanotubes that are in focus in the image plane. As such, strongly fluorescing out-of-focus SWCNTs are unwantedly also selected (see Section S3.2 and Figure S12 in the Supporting Information for some examples). Lastly, the Otsu threshold sometimes also disconnects two pieces of a single SWCNT, where the intermediate pixels have a lower emission intensity. The latter can be solved by applying postsegmentation improvements (see Supporting Information Section S3.5), though this does not solve the inclusion of weakly emitting SWCNTs in the statistics that are missed in the first place. Therefore, in a second approach, we trained a CNN to segment the SWCNTs.

The CNN consist of a standard U-net architecture,[51] comprising both encoding (down-sampling) and decoding (up-sampling) steps, which is typically used to classify the different pixels of an image in different classes.[51,53,54] We furthermore replaced the convolutional layers by residual blocks, which helps solving the problem of a vanishing gradient when more layers are added, such that weights of the first layer are correctly updated in the back-propagation.[55] We tested various CNNs with different encoder depths and with or without the residual blocks, and found an encoder depth of two with residual blocks sufficient to train our network for SWCNT segmentation (given the training images are only 48 × 48 pixels further down sampling is not needed). The output consists of a pixel-wise labeled image with 3 classes: "in-focus SWCNT", "out-of-focus SWCNT", and "background", where the "in-focus SWCNT" pixels are selected for further spectroscopic analysis. Sections S3.3 and S3.4 provide more details on the training and implementation of this network, while Figure S13 provides a schematic representation of the network.

Before spectroscopic analysis, a final morphological improvement was also performed, where one-pixel holes between two SWCNT segments (originating from a strong intensity

https://doi.org/10.1021/acsnano.4c02226
ACS Nano 2024, 18, 14532−14545

variation along the length of an individual SWCNT) were filled and contiguous sets of SWCNT pixels are grouped together to form an individual SWCNT (see Supporting Information Section S3.5 and Figure S17), resulting in a typical image segmentation as presented in Figure 4a, in which each individual segmented SWCNT is represented by a different color.

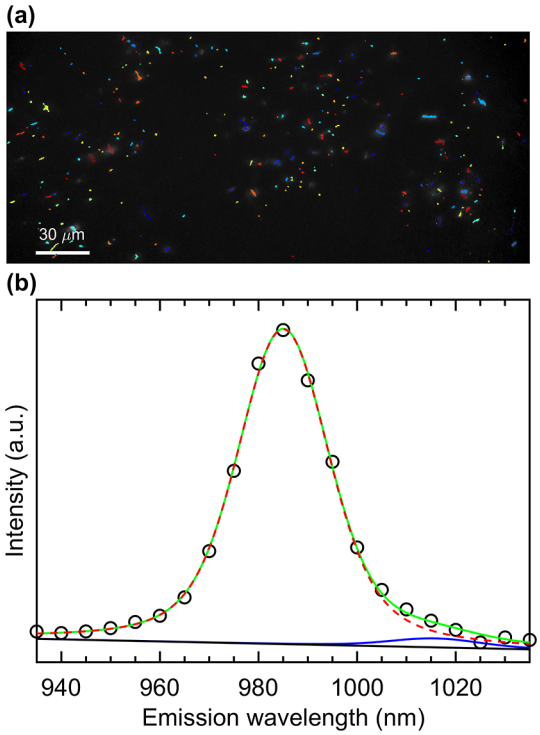

Figure 4. (a) Example HSI, represented by summing over all the spectral bands, in which the automatically identified SWCNTs are highlighted with a false, arbitrary color (see Figure S18a in the Supporting Information for an enlarged version of this figure). (b) Single-tube PL spectrum (black circles) and resulting fit (green solid line) with a sum of two Voigt lineshapes, i.e., one for the S_{11} transition (red dashed line) and one for the RBM phonon sideband (blue solid line), and a linear function in energy (gray solid line) as the background.

While segmentation can be achieved using PCA and the Otsu threshold without the CNN, much more SWCNTs can be segmented when applying the CNN. Figure S18 in the Supporting Information compares the image segmentation for three different cases, (a) using the PCA with Otsu threshold, (b) using the PCA and subsequent CNN, and (c) using the CNN without preapplying the PCA analysis. Using the same data set, the CNN segments 18,722 tubes (with PCA) and 18,472 tubes (without PCA), but the PCA with Otsu threshold only segments about 4500 tubes, some of those corresponding even to out-of-focus SWCNTs. Thus, the CNN dramatically enhances the statistical data set by more than a factor of 4. Since PCA is not computationally demanding, we furthermore opted to use it before applying the CNN as this allows to segment slightly more SWCNTs, but it could also be omitted as a step without harming the statistics too much.

Extracting PL Peak Positions and Line Widths. While in principle PL spectra are available for each pixel in the image, and thus information is available along the length of each individual segmented SWCNT, in the following example, we chose to sum the PL spectra of all pixels belonging to a single SWCNT image, thereby improving the signal-to-noise ratio significantly (see Figure 4b for an example). This could be done since in the current example, having SWCNTs coated with 1 wt/V % DOC in a 20 wt/V % TMOS gel and thus still having 80% of surrounding water, the emission energy did not change along the length of the SWCNT, and all SWCNTs are either entirely empty or entirely filled. An example of the PL spectra of individual pixels along the length of the SWCNTs is presented in Figure S19 in the Supporting Information. After applying a proper Jacobian conversion from wavelength to energy,[56] these single-tube PL spectra are then fitted using a sum of two Voigt functions, corresponding to the S_{11} excitonic peak and the radial breathing mode (RBM) phonon sideband, respectively,[8] combined with a linear background to account for any remaining baseline deviations in the spectra. To reduce the number of fit parameters, the position of the RBM phonon sideband was set at a fixed energy for each chiral species with respect to the main emission peak, as determined by Raman spectroscopy, e.g., to be 38.2 meV for the (6,5) SWCNT, and with the same fwhm and line shape as that of the main excitonic peak, such that only the relative amplitude of this phonon sideband is a fit parameter. An example of such a fit is shown in Figure 4b (note that the fit is performed using an energy axis; while Figure 4b presents the as-measured PL spectra in wavelength). After fitting, the PL peak emission energy, the fwhm of the peak, and the intensity of the PL spectrum are stored for further statistical analysis. First, all fitted parameters corresponding to other chiralities, in particular the (8,3) and (6,4) chirality are removed from the statistics (corresponding to less than 6.5% of the data in the example presented in the next section, mainly due to the highly pure chirality-sorted samples used). Second, to avoid significant outliers from wrongly fitted spectra, i.e., due to the large statistics it is impossible to check every spectrum with its corresponding fit, we removed all data with a too narrow or too broad line width (typical line widths are 20−30 meV, while fits with line widths below 6 meV or above 80 meV were removed from the statistics, corresponding to approximately 5% of the data). Moreover, after doing proper fit error analysis, effectively reducing the number of degrees of freedom to two times the number of crossing points of the fit and the experimental data, fits with line width errors above 5 meV (i.e., >1/4th of the line width itself) were also removed from the statistics. This selection, combined with the previous ones removes about 40% of the segmented SWCNTs.

Hyperspectral Imaging of Chirality-Enriched, Empty, and Water-Filled Sorted SWCNTs. In previous ensemble studies, specifically sorted SWCNT samples were necessary in order to resolve the environment-specific PL.[4,8−10,18−21] Although the single-tube approach of the hyperspectral microscopy setup can overcome this limitation, only when sorted SWCNTs are studied, the possibly probed variations in the PL can be unambiguously assigned to specific environment-induced interactions. Therefore, (6,5)-enriched and empty and water-filled sorted SWCNT samples were prepared[23,39] and investigated as the different chiralities and the empty or water-filled nanotubes are expected to introduce the majority of the PL variations.

These sorted samples were prepared from SWCNTs synthesized by the high pressure carbon monoxide method (HiPco),[57] which were dispersed in heavy water (D_2O) using 10 g/L sodium DOC by gentle magnetic stirring.[3] Ultra-

https://doi.org/10.1021/acsnano.4c02226
ACS Nano 2024, 18, 14532−14545

sonication was strictly avoided in order to preserve the nanotube's length and to minimize the unintended opening and, consequent, filling of the SWCNTs.[13] After centrifugation, the so-called parent SWCNT sample was collected, which contains many different chiralities, including (6,5), according to absorption spectroscopy (more details can be found in Section S5 of the Supporting Information).

Next, the parent SWCNT sample was sorted to the (6,5)-chirality via a known ATPE methodology, focusing mostly on attaining a high (6,5) concentration with minimal chiral impurities in the investigated wavelength range so that the observed SWCNTs can be unambiguously related to (6,5) SWCNTs.[39] The resulting (6,5) enrichment of this ATPE sample is verified by means of absorption spectroscopy (Figure S20 of the Supporting Information).

In this chirality-enriched sample, mostly the difference between the naturally present closed (empty) and opened (water-filled) (6,5) SWCNTs is expected to define the SWCNT emission wavelength and line width.[8] In order to be able to assign these expected spectral shifts unambiguously to either the empty or the water-filled SWCNT PL, the two species were separated from each other using DGU, where depending on the filling state the nanotubes will reside at a different height in the ultracentrifuge tube after DGU due to their differences in buoyant density.[18,23] By probing RBMs of the two species with in situ RRS, measuring directly in the ultracentrifuge tube, their distributions can be monitored as a function of depth in the ultracentrifuge tube, allowing for their identification and subsequent collection.[23] The results of the in situ RRS characterization of this DGU separation, measured in resonance with the (6,5) SWCNTs (568 nm), show, first, that the water-filled SWCNTs are more abundant (if assuming similar Raman cross sections and resonance conditions), despite the careful dispersion, and, second, that the empty and the water-filled SWCNT density distributions strongly overlap (see the left panel of Figure S21 of the Supporting Information). This is expected due to the fact that the (6,5) SWCNTs are just large enough to fit one single row of water molecules, while the buoyant density of the SWCNTs is determined by the encapsulated water, the SWCNT itself and the surrounding surfactant and hydration layer.[23] Based on these in situ results, the top part of the empty SWCNT fraction was collected, which still contains a non-negligible amount of water-filled SWCNTs. Therefore, this fraction was DGU sorted a second time to reduce this amount of overlapping water-filled (6,5) tubes, successfully resulting in more pure fractions of each species (see the right panel of Figure S21 of the Supporting Information). At the end of this two-step DGU process, an empty SWCNT fraction, a water-filled SWCNT fraction, and a mixed SWCNT fraction, where the distributions of both species overlap, were collected. These fractions are referred to as the (6,5)-E, the (6,5)-W and the (6,5)-M sample, respectively.

To verify the correct separation of the empty and the water-filled (6,5) SWCNT in the obtained (6,5)-E/M/W samples, they were characterized with high-resolution RRS at 568 nm. The resulting spectra, presented in Figure 5 after normalization, were fitted simultaneously, meaning that the fit parameters of the empty and the water-filled (6,5) RBMs have been optimized to fit all three spectra. Only the peak amplitudes were allowed to vary, so that the difference in abundance between the empty and the water-filled SWCNTs in each of the samples could be assessed, resulting in the

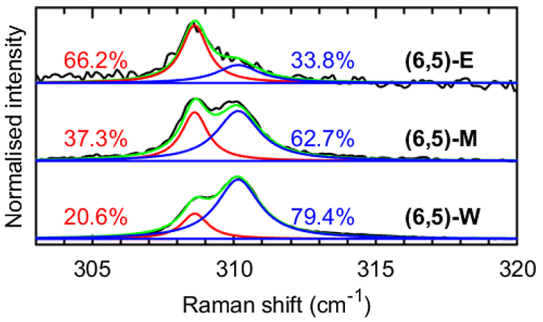

Figure 5. Normalized Raman spectra (black), recorded at 568 nm, of the (6,5)-E, the (6,5)-M, and the (6,5)-W samples demonstrate together with their simultaneous fits (green) the successful separation of the empty (red) and the water-filled (blue) (6,5) SWCNTs in the samples. The percentages next to each peak denote the relative fitted amplitude of the empty (red) and the water-filled (blue) SWCNT component. These amplitudes cannot be interpreted as the actual concentrations, as the difference in resonance behavior and Raman cross-section between the two species are not taken into account.

abundance percentages that are placed next to each peak in Figure 5. Note that although these percentages give a good indication, they do not represent an accurate quantification of the actual abundance, as the difference in Raman cross section and the shift in resonance upon water filling are not taken into account. Nevertheless, these abundances confirm the good separation of empty from water-filled SWCNTs, and since we use the same excitation wavelength as in the hyperspectral imaging, they are a good representation of the excited species observed in the HSIs. Indeed, even the absorption spectra of the (6,5)-E/M/W samples show an apparent redshift of the (6,5) SWCNTs' first order optical transition (S_{11}) due to the increasing amount of water-filled SWCNTs among the samples (see Figure S22 of the Supporting Information).

Lastly, despite the high quality and purity of these samples, these separation steps and the initial low abundance of empty SWCNTs caused the (6,5)-E sample to be very low in concentration, as can be seen by comparing the signal-to-noise ratios of the normalized Raman spectra in Figure 5 or from the absorption spectra (Figure S22). Although this can possibly complicate its ensemble characterization, this poses no problem for the following hyperspectral imaging analysis study, as any sample must anyway be amply diluted to be able to spatially resolve individual SWCNTs in the HSIs.

Statistical Analysis of the (6,5)-E/M/W Samples. To obtain statistically relevant information on the environment-induced variations in the PL of the individual SWCNTs in the (6,5)-E/M/W samples, ∼50 HSIs of each sample were acquired. These HSIs were taken at random positions in the microscope samples in a wavelength range covering the (6,5) PL (935−1035 nm, with 5 nm increments). The single-tube PL for all the individual SWCNTs was extracted from the HSIs using the above-described automated analysis procedure. In total 5444, 5372, and 7906 SWCNTs were imaged in the (6,5)-E/M/W samples, respectively.

To compare the PL properties of the individual SWCNTs among the different (6,5) samples, bivariate histograms are constructed as a function of fwhm and peak emission energy. Figure 6 presents the bivariate histograms for the three different samples with the color scale representing the number of nanotubes with emission energy and fwhm within one

https://doi.org/10.1021/acsnano.4c02226
ACS Nano 2024, 18, 14532−14545

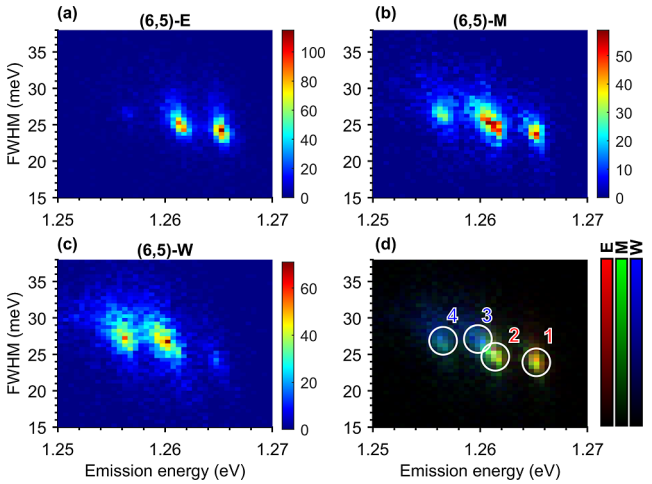

Figure 6. (a–c) Bivariate histograms as a function of the fitted emission peak energy and fwhm of the single-tube spectra of the (a) (6,5)-E (5444 tubes), (b) (6,5)-M (5372 tubes), and (c) (6,5)-W samples (7906 tubes). The color scale indicates the number of nanotubes within each bin and each histogram is presented between '0' and the maximum number of counts in one bin. Data is presented into bins with 0.5 meV width. (d) False color histogram, constructed by overlaying the normalized bivariate histograms of the (6,5)-E (red), the (6,5)-M (green), and the (6,5)-W (blue) sample in each a different color. Four distinct peaks can be recognized and, moreover, assigned based on their color to the empty (6,5) SWCNT PL (peaks 1 and 2) and to the water-filled (6,5) SWCNT PL (peaks 3 and 4).

specific bin. Thus, one count corresponds to one specific SWCNT, each being composed of a number of segmented pixels as mentioned previously. In Figure 6d, the three bivariate histograms of the (6,5)-E/M/W samples are overlaid after proper normalization, where the histogram of each sample has been assigned a different color. Doing so reveals four distinct peaks in the bivariate histograms of the samples, indicated by the white circles in Figure 6d. Based on the color of these peaks in this false color histogram, their origin can be assigned. Indeed, as the first two peaks are red/orange, they must originate from overlapping peaks of the (6,5)-E (red) and the (6,5)-M (green) sample. Since only empty (6,5) SWCNTs are abundant in the first sample due to previous separations, these peaks can be assigned to the empty (6,5) SWCNT PL. Similarly, peaks 3 and 4 are cyan-like colored, meaning that this PL comes from the (6,5)-M (green) and the (6,5)-W (blue) sample and, hence, must be from the water-filled (6,5) SWCNTs. Note that since we never observe SWCNTs that are partially filled (Figure S19), which is due to the specific sample conditions where SWCNTs are embedded in a gel matrix with excess water in line with previous results,[8] only contributions of fully empty or fully filled SWCNTs can appear in the histogram. Besides the empty and the water-filled SWCNT PL peaks, the hyperspectral microscopy thus resolves an additional splitting of the PL of both the empty and the water-filled (6,5) SWCNTs. The origin of the two PL peaks for (6,5) SWCNTs with the same inner environment can be assigned to the (6,5) enantiomers that are expected to be present in these samples.[19−22] Indeed, as the SWCNTs studied here are dispersed with the natural bile salt surfactant DOC, which is a chiral (and enantiopure) molecule by nature, it is expected to stack itself differently around left- and right-handed nanotubes of the same chirality. This is well-known to result in the ability to separate these two enantiomers from each other in DGU[21] and ATPE.[22,39] Moreover, this different wrapping results in a slight change of the nanotube's outer environment, which in turn, can affect the PL properties,[22] hence explaining why two peaks are observed in Figure 6 per inner environment type.

The exact peak positions and, hence, the PL properties of these empty (E^- and E^+) and water-filled (W^- and W^+) (6,5) SWCNT enantiomers (where the "−" and "+" are arbitrarily assigned), are determined by fitting the three histograms with a sum of four bivariate Gaussian functions, one for each (6,5) species, where the emission energy and the fwhm are assumed to be normally distributed around the bins with the maximum intensity in the histograms. These fits have been performed simultaneously, meaning that the parameters of each Gaussian function, except for the amplitude, are identical for the three histograms of the (6,5)-E/M/W samples. Note that the peaks in Figure 6 seem slightly tilted due to an anticorrelation between the fwhm and the emission energy. Therefore, an additional correlation parameter, ρ, that is optimized for all four peaks together is included in the bivariate Gaussian functions (see Methods for the definition of ρ). The results of this simultaneous fit are presented in Figure 7, where the peak positions and their 1σ errors are overlaid in black or white. From Table 1 it can be deducted that the shift between E^- and W^- peaks is 5.186 ± 0.055 meV and between E^+ and W^+ peaks amounts to 5.378 ± 0.055 meV, in line with the previously observed 4.99 ± 0.46 meV red-shift for water-filled versus

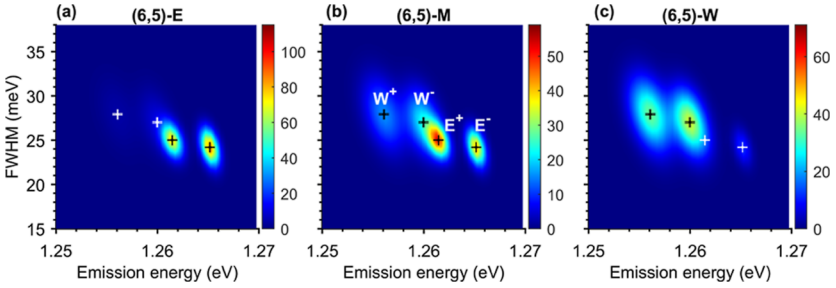

Figure 7. Simultaneous fit of the bivariate histograms of the (a) (6,5)-E, (b) the (6,5)-M, and (c) the (6,5)-W samples, plotted with the same color scale and emission and fwhm ranges as in Figure 6, revealing the accurately determined PL peak positions and line widths for the empty (E^- and E^+) and the water-filled (W^- and W^+) (6,5) SWCNTs (see also Table 1). The peak parameters are optimized to fit all three histograms at once and obtained peak positions are plotted with their 1σ fit errors (in white or in black, where the color was only chosen to distinguish them better on top of the color maps). The correlation between the line width and the emission wavelength is taken into account through a single parameter, $\rho = -0.403 \pm 0.018$, equal for all four peaks and for the three maps.

https://doi.org/10.1021/acsnano.4c02226
ACS Nano 2024, 18, 14532−14545

Table 1. Overview of the Fitted Mean (μ) and Standard Deviations (σ) of the Energy and fwhm With Their 1σ Fit Errors of the Bivariate Gaussian Functions and Their Errors for the Four Peaks Present Throughout the Three Bivariate Histograms, Originating From the PL of the Empty and the Water-Filled (6,5) SWCNT Enantiomers[a]

	μ_E (eV)	σ_E (meV)	μ_{fwhm} (meV)	σ_{fwhm} (meV)
E^-	1.265161 ± 0.000014	0.606 ± 0.014	24.203 ± 0.033	1.416 ± 0.032
E^+	1.261452 ± 0.000021	0.678 ± 0.020	25.003 ± 0.038	1.319 ± 0.037
W^-	1.259975 ± 0.000053	1.163 ± 0.048	27.017 ± 0.084	2.458 ± 0.066
W^+	1.256074 ± 0.000051	1.356 ± 0.052	27.919 ± 0.080	2.758 ± 0.078

[a]The correlation parameter was found to be equal to $\rho = -0.403 \pm 0.018$ (see Methods for a definition of the parameters, and Table 2 for the fitted amplitudes of each peak).

empty (6,5) SWCNTs in ensemble spectroscopy after DGU sorting of both species.[10] While a 11.6% line broadening of water-filled versus empty (6,5) SWCNTs can be observed at the single-tube level, ensemble spectroscopy previously showed a 35% increase in line broadening for (6,5) SWCNTs upon filling with water,[10] indicating that in the latter case the broadening is a combination of the broadening of the intrinsic line width and an additional inhomogeneous broadening due to the broader statistical distribution, as indicated by the nearly doubled standard deviations for the water-filled SWCNTs for both the emission energy and the fwhm (see Table 1). To verify whether the resulting single-tube PL data sets are also representative for the ensemble SWCNT PL properties of each sample, the sum over all single-tube PL spectra is compared with the ensemble PL spectra. The two show a good agreement for the (6,5)-E/M/W samples, hereby confirming that the single-tube PL statistics are indeed representative (see Figure S23 of the Supporting Information).

Also the very small difference between left- and right-handed enantiomers can thus be resolved, amounting to 3.709 ± 0.025 and 3.901 ± 0.074 meV for empty and water-filled SWCNTs, respectively, in line with the earlier reported shifts for enantiomer-sorted and surfactant-wrapped SWCNTs studied on the ensemble level.[19,21,22] Such shifts are only accessible in ensemble PLE spectroscopy after proper enantiomer sorting, while the samples in this work clearly contain racemic mixtures of both, showing that hyperspectral imaging can access these shifts without the need for chiral sorting.

Interestingly, from the fits of these bivariate histograms, we can not only deduce peak positions, line widths, and standard deviations for the different species, but we can also directly count the number of empty or water-filled or left- and right-handed SWCNTs present in a particular sample, by comparing the amplitudes of the four Gaussian components in the fits. As such, hyperspectral imaging is particularly promising as a quantitative characterization technique to quantify the purity in enantioselective sorting or filling-based sorting methods in an absolute way, by counting the number of tubes belonging to a specific subspecies, for which no reliable absolute methods exist to date. For example, current ensemble methods such as circular dichroism are typically calibrated relative to the highest reported observations,[19,22] and empty versus water-filled SWCNT determinations suffer from unknown but changing absorption and PL cross sections,[10] and can, therefore, not provide an accurate absolute measure of the enantiomeric purity and/or filling state. Table 2 contains the fitted percent contributions for each of the 4 peaks in the three different samples. For example, we find that the (6,5)-E sample contains 77.2 ± 1.0% of empty SWCNTs, while the (6,5)-W sample contains 95.3 ± 1.3% of water-filled SWCNTs. These percentages are quite different from the Raman scattering

Table 2. Fitted Contributions of Each of the Different Peaks in the 3 Different Samples Based on a Fit of the Bivariate Histograms Representing Counts on the Intensity Scale (Figures 6 and 7)

	(6,5)-E (%)	(6,5)-M (%)	(6,5)-W (%)
E^-	41.85 ± 0.75	18.62 ± 0.46	4.15 ± 0.30
E^+	35.30 ± 0.72	19.65 ± 0.51	0.52 ± 0.34
W^-	14.74 ± 0.93	32.18 ± 0.89	45.41 ± 0.89
W^-	8.11 ± 0.93	29.54 ± 0.88	49.91 ± 0.95

results presented in Figure 5, though previous work has shown that the Raman cross sections of empty and water-filled SWCNTs can be very different, up to a factor of 4−5 for specific chiralities (not determined for (6,5) yet).[18] Future studies could focus on quantifying such Raman cross sections through comparison with hyperspectral imaging, by comparing these counting-based distributions with wavelength-dependent Raman spectroscopy performed on the same samples. When comparing the contributions of − and + empty and water-filled SWCNTs, slight differences can be observed, most likely originating from an unintentional enantiomer sorting in the DGU and ATPE procedures. Figure S28 in the Supporting Information shows the bivariate histograms of the parent ATPE sample before DGU sorting, indeed also there showing slightly different contributions of the two enantiomers. Future studies on enantiomer-sorted SWCNTs and comparison to macroscopic circular dichroism spectroscopy will need to be conducted to verify this.

One could argue that the imaged SWCNTs have a quite broad length-distribution, ranging from one single pixel up to several tens of pixels, such that a counting based on number of CNTs is not preferred. Moreover, the lengths of empty and water-filled SWCNTs could be quite different in different samples. However, one can also obtain a good estimate of the length of each SWCNT from the HSIs. Indeed, after segmentation, the SWCNT skeleton and the end points of the SWCNT can be determined. The distance between these end points then represents the length of the segmented SWCNT, which can be further corrected to the empirical length of the SWCNT (see Section S7 in the Supporting Information and Figure S24), within our spatial resolution. Figure S25 presents the length distributions of the different samples, showing clearly a peak at 1 μm, with a small fraction of SWCNTs showing lengths beyond 8 μm. Instead of plotting the counts as the color scale in the bivariate histograms, it is therefore also possible to plot a bivariate histogram in which the color scale is weighted by the SWCNT lengths, so that the color of each bin represents the mass fraction of SWCNTs in that bin. Even though this can only be done with the above-mentioned spatial accuracy, it should provide a better

https://doi.org/10.1021/acsnano.4c02226
ACS Nano 2024, 18, 14532−14545

quantitative measure for the abundance of each of the 4 different species in each sample. Section S8 in the Supporting Information provides an overview of these weighted bivariate histograms and their corresponding fits. Given the very similar length distributions in all three samples, this weighting does not seem to influence the relative contributions of the four different peaks significantly, nor any of the other fit parameters, with variations on the specific percentages of each contribution much smaller than the error bar on the determination of these percentages. Nevertheless, when comparing samples from different origins (e.g., different synthesis methods), such a length weighting might be important to be used.

Finally, to compare with the macroscopic, ensemble PL measurements, which are measuring the averaged PL intensity of the contributing SWCNTs, the contribution of each single-tube PL spectrum to these histograms could be weighted by its PL intensity relative to the total PL intensity of that sample, determined by summing over all the single-tube PL intensities of that particular sample. Hence, the colors of the bins in the bivariate histograms shown in Figure S27 represent the percentage that a specific bin contributes to the macroscopic PL. Interestingly, although the relative fractions of each of the different components hardly change, the standard deviation of the fwhm values decreases significantly, indicating that those having a larger deviation from the mean value must have a lower PL emission intensity.

Note that in the end, having the parameters of the 4 different distributions defined, a measurement of a non-DGU-sorted sample was also performed, showing that the DGU sorting is not required to visualize the contributions of empty and water-filled enantiomers (see Section S9 in the Supporting Information). This demonstrates the large potential of hyperspectral imaging as a quantitative counting-based technique for estimating the purity of semiconducting SWCNT samples in terms of chiral species, filling content and enantiomeric purity.

CONCLUSIONS

Through a hyperspectral microscopy setup combined with automated SWCNT segmentation and data analysis, we are able to spatially and spectrally resolve the near-infrared PL of many individual SWCNTs simultaneously and automatically. This setup enables to resolve the inner and the outer environment-induced variations in the single-tube PL among the different SWCNTs that are otherwise obscured in the inhomogeneously broadened PL spectra measured with ensemble PLE spectroscopy. Indeed, by acquiring a set of statistically significant HSIs for surfactant-wrapped, empty-, and water-filled-sorted, (6,5)-enriched SWCNT samples, followed by an automated hyperspectral analysis, the redshift and line broadening of the PL upon water filling is verified at the single-tube level. More importantly, this hyperspectral setup and study actually reveals two PL peaks for both the empty and the water-filled (6,5) SWCNTs, which arises from the two SWCNT enantiomers inherently present in the samples that are wrapped differently by the chiral DOC surfactant molecules. Hence, unlike ensemble spectroscopic techniques, which require arduously sorted SWCNT samples, the hyperspectral microscopy setup presented here can readily access the single-tube properties for macroscopic quantities, even directly in nonsorted samples, allowing for unravelling the environment-dependent optical properties of individual SWCNTs. Moreover, a very large statistical data set that can be obtained by this automated image acquisition, SWCNT segmentation, and analysis, allows to quantify the abundance of a specific species (e.g., different filling states, different enantiomers) by simple counting of the number of observed tubes of each species, providing an absolute method for assessing enantioselective chiral sorting methods.

METHODS

Hyperspectral Microscopy Setup. The SWCNTs in the microscope's sample plane are excited with a continuous wave optically pumped semiconducting laser with a wavelength of 568 nm and maximum power of 200 mW (Sapphire 568 LP, Coherent). This is done in a wide-field manner by focusing the first expanded laser beam (30 mW) on the back focal plane of the microscope's objective, resulting in an excitation intensity of approximately 7 W/cm^2. Although the polarization direction of the linearly polarized light of the laser compared to the SWCNT orientation in the sample influences the excitation efficiency, since the SWCNTs are all oriented randomly, this effect is compensated for by acquiring a sufficiently large sample size. The generated SWCNT PL is imaged by an inverted, infinity-corrected, epifluorescence microscope (Eclipse, Ti−U, Nikon), equipped with a brightfield, oil-immersion objective with a magnification of 60 and numerical aperture of 1.4 (CFI Plan Apo Lambda 60x Oil, Nikon) and a 775 nm long-pass filtercube. The resulting microscope images are filtered by a LCTF (VariSpec LNIR, 850−1800 nm) with a varying bandwidth (7−25 nm, see Figure S3 in the Supporting Information) to allow for the wavelength-dependent image acquisition with a liquid-nitrogen-cooled, two-dimensional, Si CCD camera (PyLoN:400BR_eXcelon, Princeton Instruments). The HSIs were recorded in the range of 935−1035 nm in 5 nm steps with 5 accumulations for each emission wavelength and an exposure time of 6 s. The wavelength-dependent background PL, including the detector's dark current, was measured analogously at a position in the microscope sample where no SWCNTs were present. The wavelength-independent flatfield was measured by spin-coating (1500 rpm, 60 s) a 10 wt/V % PMMA (120 kDa, Sigma-Aldrich) solution in dichloromethane (99.8%, Acros Organics) containing 1 mM IR-140 (5.5′-dichloro-11-diphenylamino-3,3′-diethyl-10,12-ethylenethiatricarbocyanine perchlorate, 95%, Sigma-Aldrich) on a coverslip. The spectral sensitivity curve was determined by recording the white-light spectrum of a calibrated halogen lamp. To this end, a stack of a few microscope slides with on top a piece of ground glass was placed in the sample holder, which was then illuminated by the halogen lamp from above. In between these glass pieces immersion oil was added to avoid interference and the stack of microscope slides was used to make sure that the ground glass was not placed in the focal plane of the objective.

Chirality Enrichment and Filling-State Separation. The (6,5)-enriched empty, mixed and water-filled samples ((6,5)-E/M/W) were prepared from SWCNTs, synthesized by the HiPco method[57] (batch 197.2) at Rice University (Houston, Texas, USA). The specific SWCNT batch used, contains a large fraction of such small-diameter SWCNTs with lengths in the μm range, ideally suited for the subsequent hyperspectral imaging.[4,58] First, these SWCNTs were gently dispersed in D_2O (99.8% AtomD, Cortecnet) using 10 g/L DOC (further denoted as 1 wt/V %) (99%, Acros Organics) at a concentration of 10 mg SWCNT powder per 3 mL surfactant solution by stirring with a small (3 × 8 mm) magnetic stir bar.[3] Ultrasonication was purposely avoided to minimize the induced defects, cutting and water filling.[13] After 6 weeks of stirring at 300 rpm, the dispersions were centrifuged for 4 h at 22 °C and an acceleration of 16,215g (Sigma 2-16KCH centrifuge, swing-out rotor). Note that this elongated methodology is applied solely to obtain sufficiently long SWCNTs for investigating the HSI along the length of the nanotubes, however, a faster procedure (e.g. using sonication) can also be used, at the cost of the length of the nanotubes. Next, after first collecting the supernatant, 3 mL of fresh surfactant solution (1 wt/V % DOC in D_2O) was added to the sediment and again magnetically stirred for more than 8 weeks in order to obtain a more

https://doi.org/10.1021/acsnano.4c02226
ACS Nano 2024, 18, 14532−14545

concentrated dispersion than the first supernatant. Finally, after this dispersion was ultracentrifuged, analogously to the first run, the supernatant was collected, which will be referred to as the parent SWCNT sample. Next, the parent sample was enriched in the (6,5) chirality using ATPE, using a similar procedure as described in ref 39. First, a solution of polyethylene glycol (PEG, 6 kDa, Alfa Aesar), dextran (DEX, 40 kDa, TCI Chemicals), sodium dodecylbenzenesulfonate (SDBS, 88%, Acros Organics), sodium cholate (SC, 99%, Acros Organics) and the parent SWCNT sample (containing 1 wt/V % DOC) was made in D_2O so that the following final concentrations are obtained per unit volume of D_2O: 11.66 wt/V % of PEG, 5 wt/V % of DEX, 1 wt/V % of SDBS, 0.5 wt/V % of SC, and 0.1 wt/V % of DOC. After thoroughly mixing the solution with a vortex mixer for 1 min, the solution was centrifuged at 5000 rpm for 3 min at a fixed angle to speed up the spontaneous separation process (MiniSpin plus centrifuge, Eppendorf). Once separated, the (6,5) SWCNT-rich bottom phase was carefully collected and fresh surfactant solution (1 wt/V % DOC in D_2O) was added to it in order to stabilize the nanotube dispersion as the final DOC concentration is too low. After ATPE, the PEG and DEX polymers as well as all other surfactants besides DOC were removed from the SWCNT sample through dialysis using an Amikon stirred ultrafiltration cell equipped with a 25 mm large 100 kDa ultrafiltration disc (Millipore). Lastly, the empty and water-filled SWCNTs in the (6,5)-enriched sample were separated from each other using a two-step DGU sorting protocol, where the fraction of empty SWCNTs is collected from the first separation and similarly sorted a second time in order to further increase the purity in empty (6,5) SWCNTs. For both DGU procedures, a low density phase (ρ = 1.186 g/mL) of the iohexol gradient medium (5-(*N*-2,3-dihydroxypropylacetamido)-2,4,6-triiodo-*N*,*N*′-bis(2,3-dihydroxypropyl) isophthalamide, trade name "Nyco-Denz", Axis-Shield) in D_2O was superimposed on top of a high-density phase (ρ = 1.221 g/mL). Both phases also contain 1 wt/V % DOC to match the surfactant concentration of the SWCNT sample. For the first DGU run, the larger volume of (6,5)-enriched SWCNTs was distributed over both density phases in 3.5 mL ultracentrifuge tubes (product number 349622, Beckman). In the second DGU run, the collected empty SWCNT fraction, still containing a non-negligible fraction of water-filled SWCNTs, was added to the low-density phase in 0.8 mL ultracentrifuge tubes (product number 103353, Beckman). The two density phases were mixed to form a quasi-linear density gradient by tilting and rotating the ultracentrifuge tubes around their long axis. During the first and the second DGU run, the ultracentrifuge tubes were centrifuged at their respective maximum centrifugation speeds, namely 236,400*g* for the 3.5 mL ultracentrifuge tubes and 200,100*g* for the 0.8 mL ones, for at least 22 h to reach isopycnic equilibrium of the SWCNTs in the gradient medium (Optima Max-XP tabletop ultracentrifuge, MLS-50 swing-out rotor, 20 °C). To monitor the separation of the empty from the water-filled (6,5) SWCNTs directly inside the ultracentrifuge tube after each DGU run, in situ RRS[23] was performed at 568 nm to probe the characteristic (6,5) RBMs by mounting the ultracentrifuge tubes on an automated translation stage (MTS50/M-Z8, Thorlabs). Based upon these results, fractions were assigned in the ultracentrifuge tubes to empty SWCNTs, water-filled SWCNTs, and a mixture of both where the two RBMs overlap. Finally, after manual collection with a syringe of the empty, mixed and water-filled (6,5) fraction of the second DGU run, the iohexol gradient medium was removed from these samples by dialysis with 1 wt/V % DOC in D_2O using 10 kDa dialysis cassettes (Slide-A-Lyzer), resulting in the (6,5)-E, the (6,5)-M and the (6,5)-W sample.

Ensemble Spectroscopic Techniques. Absorption spectra were taken over a wavelength range from 200 to 2500 nm using a Cary 5000 UV−vis-IR spectrometer in 60 μL quartz microcells with path lengths of 3 mm. The spectra were baseline corrected with a 1 wt/V % DOC/D_2O solution. Due to the saturated D_2O absorption band this correction induces a noise band around 2000 nm, yet far separated from the (6,5) absorption spectra. RRS was performed with a Dilor XY800 triple spectrometer in backscattering geometry equipped with a liquid-nitrogen-cooled CCD detector. The sample was illuminated with a dye laser (Spectra-Physics, model 375), filled with rhodamine 110 and pumped by a 5 W Ar^+-laser (Spectra-Physics, model 2020), tuned to 568 nm. All of the Raman spectra were corrected for the setup's spectral sensitivity and the spectrometer's wavelength calibration. The (6,5) RBM peak in the Raman spectra of the (6,5)-E/M/W samples was fitted with a sum of two Lorentzian functions, one for each filling state. Since in all the spectra of the three samples, the same peak components are present, all parameters of these functions, except for the amplitudes, were kept the same for all three samples.

Microscope Sample Preparation. SWCNT samples for the hyperspectral microscopy setup were prepared from the (6,5)-E/M/W samples by first diluting them so that individual SWCNTs can be visualized ((6,5) S_{11} peak absorbance of ~3×10^{-3} in 3 mm optical path length cells). Next, the sol−gel precursor TMOS (99%, Acros Organics), which hydrolyzes in contact with water, forming as such a silica gel network[43] (see Section S4 in the Supporting Information), was mixed in the SWCNT samples at a ratio of 20 V %. After 2 min, the supernatant excess of TMOS, not miscible in D_2O, was removed. The remaining bottom part was left to condensate for 15 min, after which a 1 μL drop was pipetted in between a microscope slide (76 × 76 × 1 mm, Marienfeld) and coverslip (24 × 50 × 0.15 mm, #1, Menzel-Gläser), resulting in a thin slab of transparent gel once the condensation was finished. Prior to pipetting, the plasma cleaned (10 min, 18 W at an ambient air flow of 23 mL/min, PDC-32G-2, Harrick Plasma (S.A.F.I.R.)) glassware were given a hydrophobic coating (Rain-X) in order to minimize the possible interactions with the hydrophilic SWCNT micelles. Finally, the microscope coverslip is sealed off with a small amount of vacuum grease to prevent drying of the sample during image acquisition.

Statistical Classification. After fitting the individual single-tube PL spectra (see main text), bivariate histograms were generated from the fitted fwhm and peak positions. The positions of the different (6,5) SWCNT PL peaks in the histogram were determined by simultaneously fitting these bivariate histograms with a sum of four bivariate and correlated Gaussian functions, $\sum_{i=1}^{4} a_i G_i\,(E_{\mathrm{em},i}, \mathrm{fwhm}_i)$. Each of these Gaussian distributions, G_i take the form

$$\frac{1}{2\pi\sigma_{E,i}\sigma_{\mathrm{fwhm},i}\sqrt{1-\rho^2}}\, e^{-\frac{1}{2(1-\rho^2)}\left(\left(\frac{E_{\mathrm{em},i}-\mu_{E,i}}{\sigma_{E,i}}\right)^2 - 2\rho\left(\frac{E_{\mathrm{em},i}-\mu_{E,i}}{\sigma_{E,i}}\right)\left(\frac{\mathrm{fwhm}_i-\mu_{\mathrm{fwhm},i}}{\sigma_{\mathrm{fwhm},i}}\right) + \left(\frac{\mathrm{fwhm}_i-\mu_{\mathrm{fwhm},i}}{\sigma_{\mathrm{fwhm},i}}\right)^2\right)}$$

where $\mu_{E,i}$ and $\mu_{\mathrm{fwhm},i}$ are the means in respectively the emission energy and fwhm dimension respectively, $\sigma_{E,i}$ and $\sigma_{\mathrm{fwhm},i}$ are the standard deviations in the same dimensions and ρ is the correlation parameter. Since in each histogram, the same four peaks are being fitted, the peak parameters ($\mu_{E,i}$, $\sigma_{E,i}$, $\mu_{\mathrm{fwhm},i}$, $\sigma_{\mathrm{fwhm},i}$) are optimized to fit all three bivariate histograms simultaneously. Similarly, ρ is optimized for all the peaks and, again, all histograms at once, resulting in a single correlation for all the (6,5) SWCNT species. The peak amplitudes, a_i, are determined through linear regression for each histogram individually and are thus not optimized iteratively.

ASSOCIATED CONTENT

Supporting Information

The Supporting Information is available free of charge at https://pubs.acs.org/doi/10.1021/acsnano.4c02226.

https://doi.org/10.1021/acsnano.4c02226
ACS Nano 2024, 18, 14532−14545

Additional details and figures on the microscope sample preparation, the hyperspectral fluorescence microscopy setup and image corrections, the CNN for semantic image segmentation, the PL along the length of an individual SWCNT, the SWCNT sorting procedures, the comparison between ensemble spectroscopy and single-tube statistics, SWCNT length distribution of the samples, and length- and intensity-weighted bivariate histograms and their fits (PDF)

AUTHOR INFORMATION

Corresponding Authors

Wim Wenseleers − *Nanostructured and Organic Optical and Electronic Materials (NANOrOPT), Department of Physics, University of Antwerp, B-2610 Antwerp, Belgium;* orcid.org/0000-0002-3509-0945; Email: wim.wenseleers@uantwerp.be

Sofie Cambré − *Nanostructured and Organic Optical and Electronic Materials (NANOrOPT), Department of Physics, University of Antwerp, B-2610 Antwerp, Belgium;* orcid.org/0000-0001-7471-7678; Email: sofie.cambre@uantwerpen.be

Authors

Maksiem Erkens − *Nanostructured and Organic Optical and Electronic Materials (NANOrOPT), Department of Physics, University of Antwerp, B-2610 Antwerp, Belgium*

Miguel Ángel López Carrillo − *Nanostructured and Organic Optical and Electronic Materials (NANOrOPT), Department of Physics, University of Antwerp, B-2610 Antwerp, Belgium*

Bea Botka − *Nanostructured and Organic Optical and Electronic Materials (NANOrOPT), Department of Physics, University of Antwerp, B-2610 Antwerp, Belgium;* Present Address: Wigner Research Centre for Physics, 1121 Budapest, Hungary; orcid.org/0000-0003-3707-3097

Zohreh Zahiri − *Visionlab, Department of Physics, University of Antwerp, B-2610 Antwerp, Belgium;* Present Address: Imec, Kapeldreef 75, 3001 Heverlee, Belgium

Juan G. Duque − *Physical Chemistry and Applied Spectroscopy (C-PCS), Chemistry Division, Los Alamos National Laboratory, Los Alamos, New Mexico 87545, United States*

Complete contact information is available at: https://pubs.acs.org/10.1021/acsnano.4c02226

Author Contributions

The manuscript was written through contributions of all authors. All authors have given approval to the final version of the manuscript.

Notes

The authors declare no competing financial interest.

ACKNOWLEDGMENTS

This work was financially supported by the European Research Council (ERC Starting Grant, ORDERin1D, 679841) and the Research Foundation of Flanders (FWO) through a PhD fellowship for M.E. (11C9220N) and projects with grant numbers G036618N and G021112N. M.A.L.C. acknowledges support from the Research Fund from the University of Antwerp through a BOF-DOCPRO4 project. The authors also acknowledge the support of the Center of Integrated Nanotechnologies (CINT, Los Alamos National Laboratory, USA) for sharing the HiPco SWCNTs.

ABBREVIATIONS

SWCNT, single-wall carbon nanotubes; PL, fluorescence; HSI, hyperspectral image; fwhm, full-width-at-half-maximum; DGU, density gradient ultracentrifugation; ATPE, aqueous two-phase extraction; PCA, principal components analysis; CNN, convolutional neural network

REFERENCES

(1) Weisman, R. B.; Kono, J. Optical Properties of Carbon Nanotubes, Part II: A Volume Dedicated to the Memory of Professor Mildred S Dresselhaus. In *Handbook of Carbon Nanomaterials*; Weisman, R. B., Kono, J., Eds.; *World Scientific Series on Carbon Nanoscience*; World Scientific, 2019; Vol. *10*.

(2) Bachilo, S. M.; Strano, M. S.; Kittrell, C.; Hauge, R. H.; Smalley, R. E.; Weisman, R. B. Structure-Assigned Optical Spectra of Single-Walled Carbon Nanotubes. *Science* **2002**, *298*, 2361−2366.

(3) Wenseleers, W.; Vlasov, I. I.; Goovaerts, E.; Obraztsova, E. D.; Lobach, A. S.; Bouwen, A. Efficient Isolation and Solubilization of Pristine Single-Walled Nanotubes in Bile Salt Micelles. *Adv. Funct. Mater.* **2004**, *14*, 1105−1112.

(4) Duque, J. G.; Pasquali, M.; Cognet, L.; Lounis, B. Environmental and Synthesis-Dependent Luminescence Properties of Individual Single-Walled Carbon Nanotubes. *ACS Nano* **2009**, *3*, 2153−2156.

(5) Sims, C. M.; Fagan, J. A. Near-Infrared Fluorescence as a Method for Determining Single-Wall Carbon Nanotube Extraction Conditions in Aqueous Two Polymer Phase Extraction. *Carbon* **2020**, *165*, 196−203.

(6) Sims, C. M.; Fagan, J. A. Surfactant Chemistry and Polymer Choice Affect Single-Wall Carbon Nanotube Extraction Conditions in Aqueous Two-Polymer Phase Extraction. *Carbon* **2022**, *191*, 215−226.

(7) Yaari, Z.; Yang, Y.; Apfelbaum, E.; Cupo, C.; Settle, A. H.; Cullen, Q.; Cai, W.; Roche, K. L.; Levine, D. A.; Fleisher, M.; Ramanathan, L.; Zheng, M.; Jagota, A.; Heller, D. A. A Perception-Based Nanosensor Platform to Detect Cancer Biomarkers. *Sci. Adv.* **2021**, *7*, No. eabj0852.

(8) Cambré, S.; Santos, S. M.; Wenseleers, W.; Nugraha, A. R. T.; Saito, R.; Cognet, L.; Lounis, B. Luminescence Properties of Individual Empty and Water-Filled Single-Walled Carbon Nanotubes. *ACS Nano* **2012**, *6*, 2649−2655.

(9) Campo, J.; Piao, Y.; Lam, S.; Stafford, C. M.; Streit, J. K.; Simpson, J. R.; Hight Walker, A. R.; Fagan, J. A. Enhancing Single-Wall Carbon Nanotube Properties through Controlled Endohedral Filling. *Nanoscale Horiz.* **2016**, *1*, 317−324.

(10) Campo, J.; Cambré, S.; Botka, B.; Obrzut, J.; Wenseleers, W.; Fagan, J. A. Optical Property Tuning of Single-Wall Carbon Nanotubes by Endohedral Encapsulation of a Wide Variety of Dielectric Molecules. *ACS Nano* **2021**, *15*, 2301−2317.

(11) Cambré, S.; Schoeters, B.; Luyckx, S.; Goovaerts, E.; Wenseleers, W. Experimental Observation of Single-File Water Filling of Thin Single-Wall Carbon Nanotubes Down to Chiral Index (5,3). *Phys. Rev. Lett.* **2010**, *104*, 207401.

(12) van Bezouw, S.; Arias, D. H.; Ihly, R.; Cambré, S.; Ferguson, A. J.; Campo, J.; Johnson, J. C.; Defillet, J.; Wenseleers, W.; Blackburn, J. L. Diameter-Dependent Optical Absorption and Excitation Energy Transfer from Encapsulated Dye Molecules toward Single-Walled Carbon Nanotubes. *ACS Nano* **2018**, *12*, 6881−6894.

(13) Wenseleers, W.; Cambré, S.; Čulin, J.; Bouwen, A.; Goovaerts, E. Effect of Water Filling on the Electronic and Vibrational Resonances of Carbon Nanotubes: Characterizing Tube Opening by Raman Spectroscopy. *Adv. Mater.* **2007**, *19*, 2274−2278.

(14) Heller, D. A.; Jin, H.; Martinez, B. M.; Patel, D.; Miller, B. M.; Yeung, T.-K.; Jena, P. V.; Höbartner, C.; Ha, T.; Silverman, S. K.; Strano, M. S. Multimodal Optical Sensing and Analyte Specificity

Using Single-Walled Carbon Nanotubes. *Nat. Nanotechnol.* **2009**, *4*, 114−120.
(15) Kim, M.; Chen, C.; Wang, P.; Mulvey, J. J.; Yang, Y.; Wun, C.; Antman-Passig, M.; Luo, H.-B.; Cho, S.; Long-Roche, K.; Ramanathan, L. V.; Jagota, A.; Zheng, M.; Wang, Y.; Heller, D. A. Detection of Ovarian Cancer via the Spectral Fingerprinting of Quantum-Defect-Modified Carbon Nanotubes in Serum by Machine Learning. *Nat. Biomed. Eng.* **2022**, *6*, 267−275.
(16) Ackermann, J.; Metternich, J. T.; Herbertz, S.; Kruss, S. Biosensing with Fluorescent Carbon Nanotubes. *Angew. Chem., Int. Ed.* **2022**, *61*, No. e202112372.
(17) Gravely, M.; Roxbury, D. Multispectral Fingerprinting Resolves Dynamics of Nanomaterial Trafficking in Primary Endothelial Cells. *ACS Nano* **2021**, *15*, 12388−12404.
(18) Cambré, S.; Wenseleers, W. Separation and Diameter-Sorting of Empty (End-Capped) and Water-Filled (Open) Carbon Nanotubes by Density Gradient Ultracentrifugation. *Angew. Chem., Int. Ed.* **2011**, *50*, 2764−2768.
(19) Ao, G.; Streit, J. K.; Fagan, J. A.; Zheng, M. Differentiating Left- and Right-Handed Carbon Nanotubes by DNA. *J. Am. Chem. Soc.* **2016**, *138*, 16677−16685.
(20) Li, H.; Gordeev, G.; Garrity, O.; Peyyety, N. A.; Selvasundaram, P. B.; Dehm, S.; Krupke, R.; Cambré, S.; Wenseleers, W.; Reich, S.; Zheng, M.; Fagan, J. A.; Flavel, B. S. Separation of Specific Single-Enantiomer Single-Wall Carbon Nanotubes in the Large-Diameter Regime. *ACS Nano* **2020**, *14*, 948−963.
(21) Ghosh, S.; Bachilo, S. M.; Weisman, R. B. Advanced Sorting of Single-Walled Carbon Nanotubes by Nonlinear Density-Gradient Ultracentrifugation. *Nat. Nanotechnol.* **2010**, *5*, 443−450.
(22) Li, H.; Sims, C. M.; Kang, R.; Biedermann, F.; Fagan, J. A.; Flavel, B. S. Isolation of the (6,5) Single-Wall Carbon Nanotube Enantiomers by Surfactant-Assisted Aqueous Two-Phase Extraction. *Carbon* **2023**, *204*, 475−483.
(23) Cambré, S.; Muyshondt, P.; Federicci, R.; Wenseleers, W. Chirality-Dependent Densities of Carbon Nanotubes by in Situ 2D Fluorescence-Excitation and Raman Characterisation in a Density Gradient after Ultracentrifugation. *Nanoscale* **2015**, *7*, 20015−20024.
(24) Paul, L. M. G.; Grahn, H. F.; James, E. B. Multivariate Images, Hyperspectral Imaging: Background and Equipment. In *Techniques and Applications of Hyperspectral Image Analysis*; Grahn, H. F., Geladi, P., Eds.; Wiley: Chichester, UK, 2007..
(25) Chang, C.-I. *Hyperspectral Data Processing: Algorithm Design and Analysis*; John Wiley & Sons, Inc.: Hoboken, NJ, USA, 2013..
(26) Dong, X.; Jakobi, M.; Wang, S.; Köhler, M. H.; Zhang, X.; Koch, A. W. A Review of Hyperspectral Imaging for Nanoscale Materials Research. *Appl. Spectrosc. Rev.* **2019**, *54*, 285−305.
(27) Tsyboulski, D. A.; Bachilo, S. M.; Weisman, R. B. Versatile Visualization of Individual Single-Walled Carbon Nanotubes with Near-Infrared Fluorescence Microscopy. *Nano Lett.* **2005**, *5*, 975−979.
(28) Fakhri, N.; Tsyboulski, D. A.; Cognet, L.; Weisman, R. B.; Pasquali, M. Diameter-Dependent Bending Dynamics of Single-Walled Carbon Nanotubes in Liquids. *Proc. Natl. Acad. Sci. U.S.A.* **2009**, *106*, 14219−14223.
(29) Nandi, S.; Caicedo, K.; Cognet, L. When Super-Resolution Localization Microscopy Meets Carbon Nanotubes. *Nanomaterials* **2022**, *12*, 1433.
(30) Crochet, J. J.; Duque, J. G.; Werner, J. H.; Lounis, B.; Cognet, L.; Doorn, S. K. Disorder Limited Exciton Transport in Colloidal Single-Wall Carbon Nanotubes. *Nano Lett.* **2012**, *12*, 5091−5096.
(31) Qu, H.; Rayabharam, A.; Wu, X.; Wang, P.; Li, Y.; Fagan, J.; Aluru, N. R.; Wang, Y. Selective Filling of N-Hexane in a Tight Nanopore. *Nat. Commun.* **2021**, *12*, 310.
(32) Cognet, L.; Tsyboulski, D. A.; Rocha, J.-D. R.; Doyle, C. D.; Tour, J. M.; Weisman, R. B. Stepwise Quenching of Exciton Fluorescence in Carbon Nanotubes by Single-Molecule Reactions. *Science* **2007**, *316*, 1465−1468.
(33) Kagan, B.; Hendler-Neumark, A.; Wulf, V.; Kamber, D.; Ehrlich, R.; Bisker, G. Super-Resolution Near-Infrared Fluorescence Microscopy of Single-Walled Carbon Nanotubes Using Deep Learning. *Adv. Photonics Res.* **2022**, *3*, 2200244.
(34) Alexander-Webber, J. A.; Faugeras, C.; Kossacki, P.; Potemski, M.; Wang, X.; Kim, H. D.; Stranks, S. D.; Taylor, R. A.; Nicholas, R. J. Hyperspectral Imaging of Exciton Photoluminescence in Individual Carbon Nanotubes Controlled by High Magnetic Fields. *Nano Lett.* **2014**, *14*, 5194−5200.
(35) Roxbury, D.; Jena, P. V.; Williams, R. M.; Enyedi, B.; Niethammer, P.; Marcet, S.; Verhaegen, M.; Blais-Ouellette, S.; Heller, D. A. Hyperspectral Microscopy of Near-Infrared Fluorescence Enables 17-Chirality Carbon Nanotube Imaging. *Sci. Rep.* **2015**, *5*, 14167.
(36) Khripin, C. Y.; Fagan, J. A.; Zheng, M. Spontaneous Partition of Carbon Nanotubes in Polymer-Modified Aqueous Phases. *J. Am. Chem. Soc.* **2013**, *135*, 6822−6825.
(37) Subbaiyan, N. K.; Cambré, S.; Parra-Vasquez, A. N. G.; Hároz, E. H.; Doorn, S. K.; Duque, J. G. Role of Surfactants and Salt in Aqueous Two-Phase Separation of Carbon Nanotubes toward Simple Chirality Isolation. *ACS Nano* **2014**, *8*, 1619−1628.
(38) Subbaiyan, N. K.; Parra-Vasquez, A. N. G.; Cambré, S.; Cordoba, M. A. S.; Yalcin, S. E.; Hamilton, C. E.; Mack, N. H.; Blackburn, J. L.; Doorn, S. K.; Duque, J. G. Bench-Top Aqueous Two-Phase Extraction of Isolated Individual Single-Walled Carbon Nanotubes. *Nano Res.* **2015**, *8*, 1755−1769.
(39) Defillet, J.; Avramenko, M.; Martinati, M.; López Carrillo, M. Á.; Van der Elst, D.; Wenseleers, W.; Cambré, S. The Role of the Bile Salt Surfactant Sodium Deoxycholate in Aqueous Two-Phase Separation of Single-Wall Carbon Nanotubes Revealed by Systematic Parameter Variations. *Carbon* **2022**, *195*, 349−363.
(40) Cambré, S.; Muyshondt, P.; Federicci, R.; Wenseleers, W. Chirality-Dependent Densities of Carbon Nanotubes by in Situ 2D Fluorescence-Excitation and Raman Characterisation in a Density Gradient after Ultracentrifugation. *Nanoscale* **2015**, *7*, 20015−20024.
(41) Yang, F.; Wang, M.; Zhang, D.; Yang, J.; Zheng, M.; Li, Y. Chirality Pure Carbon Nanotubes: Growth, Sorting, and Characterization. *Chem. Rev.* **2020**, *120*, 2693−2758.
(42) Lichtman, J. W.; Conchello, J. A. Fluorescence Microscopy. *Nat. Methods* **2005**, *2*, 910−919.
(43) Duque, J. G.; Hamilton, C. E.; Gupta, G.; Crooker, S. A.; Crochet, J. J.; Mohite, A.; Htoon, H.; Obrey, K. A. D.; Dattelbaum, A. M.; Doorn, S. K. Fluorescent Single-Walled Carbon Nanotube Aerogels in Surfactant-Free Environments. *ACS Nano* **2011**, *5*, 6686−6694.
(44) Santos, S. M.; Yuma, B.; Berciaud, S.; Shaver, J.; Gallart, M.; Gilliot, P.; Cognet, L.; Lounis, B. All-Optical Trion Generation in Single-Walled Carbon Nanotubes. *Phys. Rev. Lett.* **2011**, *107*, 187401.
(45) Model, M. Intensity Calibration and Flat-Field Correction for Fluorescence Microscopes. *Curr. Protoc. Cytom.* **2014**, *68*, 10.14.1−10.14.10.
(46) Mohanty, J.; Palit, D. K.; Mittal, J. P. Photophysical Properties of Two Infrared Laser Dyes-IR-144 and IR-140: A Picosecond Laser Flash Photolysis Study. *Proc. Indian Natl. Sci. Acad.* **2000**, *66*, 303−315.
(47) Vidal, M.; Amigo, J. M. Pre-Processing of Hyperspectral Images. Essential Steps before Image Analysis. *Chemom. Intell. Lab. Syst.* **2012**, *117*, 138−148.
(48) Amigo, J. M.; Babamoradi, H.; Elcoroaristizabal, S. Hyperspectral Image Analysis. A Tutorial. *Anal. Chim. Acta* **2015**, *896*, 34−51.
(49) Jolliffe, I. T.; Cadima, J. Principal Component Analysis: A Review and Recent Developments. *Philos. Trans. R. Soc., A* **2016**, *374*, 20150202.
(50) Otsu, N. A Threshold Selection Method from Gray-Level Histograms. *IEEE Trans. Syst. Man Cybern.* **1979**, *9*, 62−66.
(51) Ronneberger, O.; Fischer, P.; Brox, T. U-Net: Convolutional Networks for Biomedical Image Segmentation. In *Medical Image Computing and Computer-Assisted Intervention - MICCAI 2015*; Navab, N., Hornegger, J., Wells, W. M., Frangi, A. F., Eds.; Springer International Publishing: Cham, 2015; pp 234−241.

https://doi.org/10.1021/acsnano.4c02226
ACS Nano 2024, 18, 14532−14545

(52) Barnes, R. J.; Dhanoa, M. S.; Lister, S. J. Standard Normal Variate Transformation and De-Trending of Near-Infrared Diffuse Reflectance Spectra. *Appl. Spectrosc.* **1989**, *43*, 772−777.
(53) Siddique, N.; Paheding, S.; Elkin, C. P.; Devabhaktuni, V. U-Net and Its Variants for Medical Image Segmentation: A Review of Theory and Applications. *IEEE Access* **2021**, *9*, 82031−82057.
(54) Kohl, S. A. A., Romera-Paredes, B., Meyer, C., De Fauw, J., Ledsam, J. R., Maier-Hein, K. H., Ali Eslami, S. M., Rezende, D. J., Ronneberger, O. A Probabilistic U-Net for Segmentation of Ambiguous Images. **2018**, Arxiv.1806.05034. 10.48550/arXiv.1806.05034.
(55) He, K.; Zhang, X.; Ren, S.; Sun, J. Deep Residual Learning for Image Recognition. In *2016 IEEE Conference on Computer Vision and Pattern Recognition (CVPR)*; IEEE, 2016; pp 770−778..
(56) Mooney, J.; Kambhampati, P. Get the Basics Right: Jacobian Conversion of Wavelength and Energy Scales for Quantitative Analysis of Emission Spectra. *J. Phys. Chem. Lett.* **2013**, *4*, 3316−3318.
(57) Bronikowski, M. J.; Willis, P. A.; Colbert, D. T.; Smith, K. A.; Smalley, R. E. Gas-Phase Production of Carbon Single-Walled Nanotubes from Carbon Monoxide via the HiPco Process: A Parametric Study. *J. Vac. Sci. Technol., A* **2001**, *19*, 1800−1805.
(58) Duque, J. G.; Parra-Vasquez, A. N. G.; Behabtu, N.; Green, M. J.; Higginbotham, A. L.; Price, B. K.; Leonard, A. D.; Schmidt, H. K.; Lounis, B.; Tour, J. M.; Doorn, S. K.; Cognet, L.; Pasquali, M. Diameter-Dependent Solubility of Single-Walled Carbon Nanotubes. *ACS Nano* **2010**, *4*, 3063−3072.

https://doi.org/10.1021/acsnano.4c02226
ACS Nano 2024, 18, 14532−14545